Sensors & Actuators: A. Physical 408 (2026) 118024

Contents lists available at ScienceDirect

Sensors and Actuators: A. Physical

journal homepage: www.journals.elsevier.com/sensors-and-actuators-a-physical

Influence of curing temperature on mechanical and viscoelastic properties of siliglass platinum silicone for Fiber Bragg Grating sensors encapsulation in flexible and wearable applications

L. Maggioni, E. Lacagnina, A. Cigada, P. Saccomandi*

Department of Mechanical Engineering, Politecnico di Milano, Via La Masa 1, Milan, 20156, Italy

HIGHLIGHTS

- Curing temperature strongly influences Siliglass' mechanical behavior.
- Higher curing temperatures reduce elongation and increase stiffness.
- Stress–relaxation depends on both curing conditions and loading parameters.
- Finite element modeling accurately predicts viscoelastic response.
- This work supports the tunability of Siliglass for biomedical and flexible electronics applications.

ARTICLE INFO

Keywords:
Siliglass
Platinum-cured silicone
Curing temperature
Mechanical properties
Viscoelastic behavior
Stress–relaxation
Finite element analysis
Fiber bragg grating sensors
Wearable devices
Soft elastomer encapsulation

ABSTRACT

Applications in flexible wearable devices and wearable electronics for health monitoring purposes often rely on soft materials whose mechanical and viscoelastic properties can be precisely tuned and controlled. Siliglass, a platinum-cured silicone, is a promising candidate due to its flexible characteristics, biocompatibility, and tunable performance. This study investigates the effect of curing temperature (25 °C, 50 °C, 75 °C) on the mechanical behavior and stress–relaxation of Siliglass. Uniaxial tensile tests revealed a strong dependence on curing conditions: elongation at break decreased from 97% to 34% as temperature increased, while Young's modulus rose by over 60%. Poisson's ratio remained close to 0.5, confirming the near incompressibility of the material. Stress–relaxation tests showed that both initial strain and strain rate significantly influence relaxation dynamics, with faster stress decay observed at higher curing temperatures. Finite element simulations help in evaluating the experimental results, confirming the consistency of the outcomes. The findings highlight the capacity for adjustment of Siliglass properties via curing temperature, suggesting the optimal one for flexible and wearable device applications.

1. Introduction

In recent years, wearable sensing devices have seen significant growth in biomedical engineering, particularly for monitoring elderly individuals, patients with chronic conditions, and athletes' performance [1,2]. The increasing demand for flexible, lightweight, and comfortable wearable sensors has driven research toward materials and designs that achieve a balance between measurement accuracy, mechanical robustness, and biocompatibility. At the same time, flexible electronics mark a shift in paradigm from rigid, silicon-based hardware to systems that can adapt to the complex geometry (e.g., human skin). These devices can withstand significant stretching without compromising their electrical properties benefiting from the integration of carbon-based nanomaterials, piezoelectrics or liquid metals into elastomeric substrates [3]. The synergy between flexible circuitry and soft sensing elements consequently allows for long-term monitoring capabilities with minimal user discomfort [4].

Wearable devices fabricated from soft, deformable materials can transduce mechanical stimuli into measurable signals [5]. These devices have been applied widely, including joint motion monitoring (e.g., elbow, knee, and ankle) [6,7] and physiological parameter detection (e.g., breathing) [8]. To accommodate deformation, various types of wearable sensors have been developed, including strain sensors based

* Corresponding author.
Email address: paola.saccomandi@polimi.it (P. Saccomandi).

https://doi.org/10.1016/j.sna.2026.118024
Received 28 January 2026; Received in revised form 17 May 2026; Accepted 21 May 2026
Available online 22 May 2026

on conductive fabrics [9], conductive polymer composites [10], and fiber-optic-based wearable strain sensors [11,12].

Fiber Bragg Grating (FBG) optical sensors are particularly promising for wearable applications. They are immune to electromagnetic interference, highly sensitive to strain and temperature, and allow multiplexing along a single fiber, enabling high-resolution and multi-parameter monitoring systems [13]. However, integrating FBG sensors into wearable devices remains challenging. Optical fibers are inherently fragile and poorly suited for high-deformation environments, necessitating encapsulation materials (e.g., polymeric or elastomeric) that provide mechanical protection without compromising sensitivity. Such encapsulation must also be soft, thin, and durable to ensure user comfort and reliable performance under dynamic and complex movements [14]. Previous studies have indeed demonstrated the encapsulation of FBGs within silicone-based elastomeric matrices, showing that such packaging improves mechanical robustness and flexibility while enabling effective strain transfer from soft substrates to the embedded gratings [15].

Among silicone elastomers, platinum-cured systems have gained prominence due to their high purity, lack of toxicity, biocompatibility, and potential for modification of mechanical properties via curing conditions [16]. Siliglass platinum silicone is an innovative example of this class, designed to provide optimized mechanical performance for wearable applications.

Curing temperature is a critical factor in the fabrication of these materials, as it directly affects cross-link density, thereby modifying the microstructure of the polymer matrix and influencing key properties such as elastic modulus, recovery after deformation, and viscoelastic behavior [17,18]. It was highlighted, in previous works, that, on other silicone systems, moderate changes in polymerization temperature can result in significant differences in mechanical strength, cyclic load response, and stress–relaxation [19]. These aspects are particularly relevant for wearable devices, which must maintain functional stability under repeated and prolonged deformation [20].

Despite growing interest, systematic studies on the relationship between curing temperature and the final properties of Siliglass platinum silicone remain limited. In particular, in-depth analyses associating cross-linking conditions with mechanical behavior and stress–relaxation are lacking, yet these parameters are essential for assessing suitability of the material for advanced applications.

Accurate characterization of the mechanical properties is indeed essential to evaluate the suitability of Siliglass as a substrate for wearable strain sensors. Traditional characterization methods, such as cross-head displacement, provide only coarse measurements, as they are affected by the motion of the entire specimen [21]. Contact strain gauges offer improved accuracy [22], but may introduce slippage or surface damage. In contrast, non-contact optical techniques, particularly surface marker tracking, enable full-field measurement of displacement and deformation, and are increasingly recommended for the mechanical characterization of elastomeric materials [23,24].

Understanding the stability of mechanical properties under constant deformation is also crucial for wearable sensors. Stress–relaxation, a common phenomenon in viscoelastic substrates such as silicones, can lead to unstable sensor signals if not properly accounted for [25]. Therefore, an ideal substrate must exhibit high flexibility, strong recovery, and minimal stress–relaxation. Siliglass is a promising material that could meet these requirements in future applications.

The core objective of this work is to systematically characterize the influence of curing temperature on the mechanical response of Siliglass platinum silicone. The novelty of this study lies in the establishment of a direct link between a manufacturing variable (i.e., curing temperature) and material stress–strain behavior, examined through uniaxial tensile and relaxation tests, and able to provide rigorous framework for optimizing Siliglass. Ultimately, these findings offer critical guidelines for enhancing the precision and durability of flexible wearable device applications.

2. Materials and methods

This section presents the materials employed and the main methodology adopted in the study. It details the preparation of the specimens and the experimental setup used for the tests. The protocols for both tensile and relaxation experiments are described, along with the procedures for determining the corresponding material properties. Furthermore, the finite element model implemented to simulate the material behavior is also presented.

2.1. Specimens preparation

The PlatSil® (i.e., Platinum Silicone[1]) Siliglass silicone rubbers kit used in this work is constituted by two parts which are the Silicone Elastomeric Base (Part A) and Silicone Elastomeric Curing Agent (Part B). The Siliglass base and curing agent were mixed in a 1:1 wt ratio, as recommended by the producer in the technical bulletin [26]. Before mixing the two parts together and pouring their mixture into the mold, both are degassed in a vacuum chamber for 10 minutes to remove all the air bubbles (Fig. 1(a). This step is fundamental to ensure a correct polymer solidification and to avoid structural defects; indeed, bubbles weaken the material, make its structure uneven, and compromise its strength and final mechanical behavior. The pouring mold is designed, for both the following described tension tests, according to the ASTM D412 Standard Test Method for Dumbbell - Type C specimens [27], as illustrated in Fig. 1(b).

In accordance with the aim of the work, the polymer mixture poured into the mold was cured at three distinct, pre-established, and controlled temperatures (i.e., 25 °C, 50 °C, and 75 °C), taking into account varying solidification time intervals based on the chosen temperature. Specifically, at T = 25 °C the mixture was cured for 120 minutes, at T = 50 °C for 80 minutes and, ultimately, at T = 75 °C for 40 minutes. The curing period was established based on a series of preliminary trials, in accordance with the guidelines provided by the manufacturer; this approach was adopted to ensure that the specimens attained suitable and reliable conditions for the subsequent experimental testing. Moreover, during the curing process, the temperature was monitored through a thermocouple, in order to ensure that it remained constant throughout the period. The solidified specimens obtained (Fig. 1(c) can be used for testing after airing for 24 hours prior to mechanical characterization, to avoid any potential ageing effects [28].

Once the specimens had been produced, a further analysis was carried out on them to ensure that all reactive groups of the two-component platinum-based silicone material are fully consumed once the curing time has elapsed, as suggested by the manufacturer's guidelines. For this, a medium wavelength infrared (MWIR, operational spectral range: 2700–5200 nm) hyperspectral imaging (HSI) system based on the Fourier Transform Infrared (FTIR) principle (Specim FX50; Specim Spectral Imaging Oy Ltd) was used.

Two different conditions were analyzed for each curing temperature (i.e., 25 °C, 50 °C and 75 °C): the first, without post-curing (i.e., after the specified curing time, which allows the material to solidify); the second, applying a post-curing phase (120 minutes at 75 °C), typically used for materials such as the one under examination, in order to remove residual silicon hydride (Si-H) groups [29]. The post-curing time and temperature were selected to balance the efficiency of this process with the dimensional integrity of the samples, as temperatures exceeding the glass transition temperature of any substrates (or close to the thermal expansion limit) can introduce residual stresses or anisotropic distortions, which are problematic for subsequent mechanical characterization [30].

From a data analysis perspective, reflectance spectra were extracted and normalized with respect to references. L1-normalization was applied to remove intensity scaling effects and emphasise the spectral shape; finally, the first spectral derivative was computed to enhance

[1] Registered trademark.

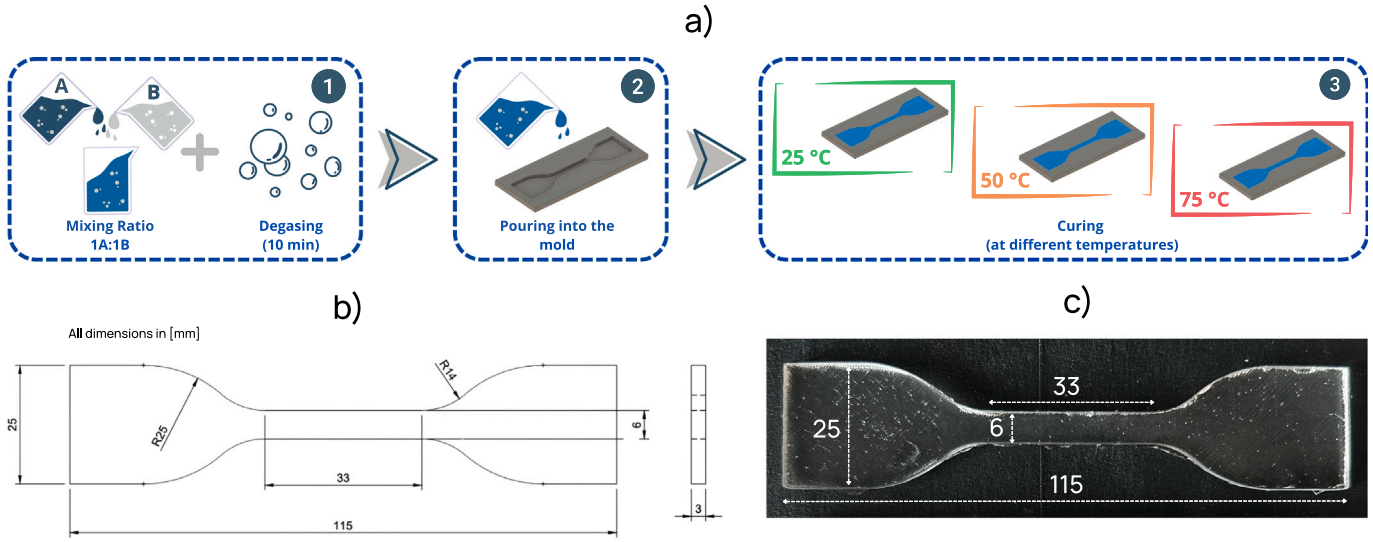

Fig. 1. Specimens' fabrication. a) Different steps for material preparation and specimens' realization: 1) Mixing Part A/Part B and degassing. 2) Pouring the mixture into the mold. 3) Curing at different temperatures. b) Dumbbell Type C specimen's dimensions according to ASTM D412. c) An example of specimen obtained after curing (T = 50 °C, in this case).

spectral variations and facilitate the analysis of residual polymerization effects, together with the extraction of the peak-to-peak amplitude in the spectral region around 2360 cm^{-1} (i.e., 4200 nm). This spectral region does not correspond to a direct absorption of the reactive Si–H or C=C groups, but rather to overtone and combination bands primarily associated with C–H vibrations. The observed changes in this region were therefore interpreted as indirect indicators of polymerization, reflecting modifications in the molecular environment and network structure resulting from the consumption of reactive groups [31].

2.2. Experimental setup

The testing activity performed under tension loading was carried out using a custom-made testing machine, presented in Fig. 2(a), and consisting specifically of a NEMA 23 SF16-04 stepper servomotor, equipped with a worm screw slide with 4 mm pitch, which ensures the imposed linear motion. A load cell with 200 N capacity was connected to an HX711 device (i.e., precision 24-bit analog-to-digital converter designed for scales to interface directly with a bridge sensor, based on Avia Semiconductor) and a UNO R3 board (Arduino UNO; Arduino), detailed in Fig. 2(b), which was selected based on the range of required force and sensitivity.

The different specimens are mounted on the machine via two Polylactic Acid (PLA) 3D-printed tensile grips (i.e., one fixed to the optical table and serving as base, the other to the moving table of the stepper motor and cohesive with the load cell), using screws to ensure constant contact pressure between gripper surface and specimen surface (Fig. 2(a), since cross-section of the specimen reduces during the test.

For strain measurements, a non-contact approach was adopted using a 2-D vision system (Fig. 2(c), equipped with a main camera (12 megapixels, 26 mm focal length, $f/1.5$ aperture, sensor-shift optical image stabilization). The sampling rate was set equal to 30 fps (i.e., frames per second), and the various frames acquired by the system were analyzed using a MATLAB code (MATLAB® 2024b; MathWorks) to obtain the actual strain in the axial and transversal directions, aided by special markers applied on the specimen itself, identifying the area of interest (i.e., useful zone), as shown in Fig. 2(d).

2.3. Mechanical characterization

In this study, the material behavior of Siliglass silicone rubber under two different tensile load conditions was fully characterized through

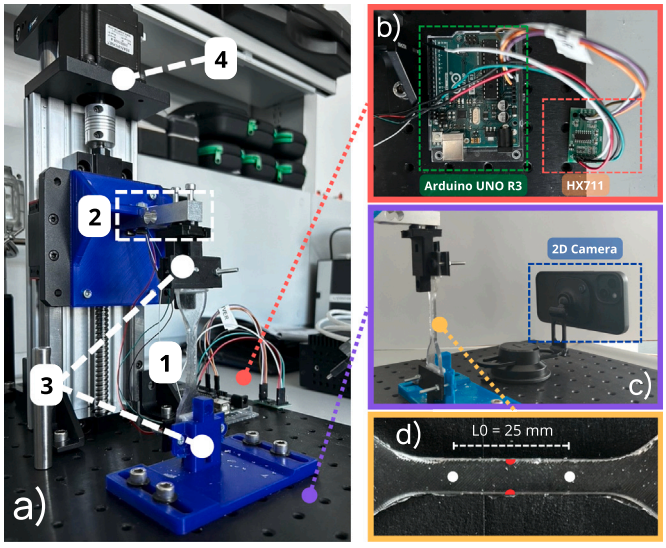

Fig. 2. Mechanical tests setup. a) Tensile testing machine used for characterization: 1) Specimen; 2) load Cell; 3) PLA 3D-printed grips; 4) Servomotor. b) Detailed view of Arduino UNO R3 board and HX711. c) Detailed view of the 2D vision system used for strain measurement. d) Zoom on the useful zone with the highlighted markers used for measuring axial (i.e., white) and transversal (i.e, red) strain. (For interpretation of the references to colour in this figure legend, the reader is referred to the web version of this article).

standardized testing procedures. Uniaxial loading test and uniaxial relaxation test were performed under quasi-static loading at room ambient conditions (i.e., T_{amb} = 25 °C, RH ≈ 42%), monitoring no significant temperature variations during the testing activities. A preload in terms of displacement equal to 0.5 mm was applied before each test.

2.3.1. Uniaxial loading test

Tension testing is one of the most common and widespread experimental typologies to assess mechanical behavior of elastomers. According to the ASTM D412, the stress/strain behavior of Siliglass material was obtained by performing uniaxial tensile loading tests [32]. In detail, all the specimens produced at different curing temperatures

were stretched up to failure under quasi-static testing speed equal to 5 mm/min.

Load values and the resulting stress data were acquired using a load cell at a sampling frequency of 10 Hz. Simultaneously, longitudinal and transverse strain data were collected via the previously described non-contact vision measurement system, with a sampling rate of 30 fps; the markers applied to the specimens facilitated the precise evaluation of strains.

This setup configuration enables the assessment of fundamental mechanical behavior parameters, including the elongation at break, which represents the maximum elongation the specimen withstands before failure and is expressed as a percentage of the original length of the test section (i.e., 25 mm), and the Ultimate Tensile Strength (UTS), which is the stress value recorded at the point of breakage. Hence, the elastic (or Young's) modulus and the Poisson's ratio are extracted by combining both stress and strain data. Elastic modulus was obtained by looking at the slope of the stress–strain curve (i.e., angular coefficient of the first-degree polynomial fitting) instead, Poisson's ratio was obtained through the common definition coming from theory:

$$\nu = -\frac{\varepsilon_t}{\varepsilon_a} \tag{1}$$

and according to the procedure described by ASTM E132 [33] and in [34,35], where ε_a and ε_t are, respectively, the longitudinal and transversal measured strain. The minus sign appears because Poisson's ratio is often positive while the transversal strain is conventionally negative (i.e., section reduction/compression). In order to assess repeatability of the data, this procedure was repeated three times (i.e., 9 tests performed in total) for each chosen curing temperature.

2.3.2. Uniaxial relaxation test

Since many elastomers exhibit viscoelastic behavior when they are normally stretched and held under a constant load in different applications, it is also important to evaluate this phenomenon for the Siliglass material, particularly when assessing the impact of curing temperature as done in this work [36]. The associated behavior could be investigated through a commonly known stress–relaxation test, where percentage stress–loss with respect to maximum stress and stress reduction over time under a constant imposed initial elongation are measured [37]. The uniaxial relaxation test was performed according to ASTM E328 [38] to evaluate both how initial imposed strain and strain speed influence the performance of the material. Siliglass specimens prepared at various curing temperatures were stretched to three different initial displacements (i.e., 2.5 mm, 5 mm, and 7.5 mm) under a constant speed of 1.5 mm/s and to an initial displacement of 1.5 mm under three different speeds (i.e., 0.5 mm/s, 1.5 mm/s, and 2.5 mm/s) and held for 600 s, as was done in a prior study [39]. Values of stress were recorded by using previous described load cell and a sample frequency of 10 Hz. Particularly, stress–loss is evaluated by computing first the Relaxation Ratio (RR) as [40]:

$$\mathrm{RR} = \frac{\sigma(t)}{\sigma_{max}} \tag{2}$$

where $\sigma(t)$ is the time history of the stress recorded by the load cell, instead σ_{max} is the maximum value of stress recorded during the respective test, and after as:

$$\mathrm{Loss} = (1 - \mathrm{RR}_{end}) \times 100 \tag{3}$$

taking the RR value at the end of the test (i.e., RR_{end}). In addition, by analyzing the stress reduction over time, it is possible to estimate the time constant τ (also known as relaxing time), which characterizes the viscoelastic behavior inherent to elastomeric materials. In practice, in this type of materials the elastic component cannot respond immediately to deformations because the viscous component slows it down. Therefore, the deformation takes place over a period, increasing exponentially until a maximum strain [41]. The same occurs in relaxation, where the material does not maintain the imposed load (or the imposed elongation) precisely, due to the same intrinsic characteristic described above [42]. The time constant of the system was estimated by applying an exponential fitting procedure to the experimental response. Specifically, the transient data were fitted with a single exponential function of the form:

$$y(t) = \mathrm{a}\ e^{-bt} \tag{4}$$

from which the time constant τ is obtained as:

$$\tau = -\frac{1}{b} \tag{5}$$

2.4. Finite element model

A finite element model (FEM) was developed in Abaqus®2025/Standard software as a tool to better interpret and verify the accuracy of experimentally obtained mechanical properties. This model was introduced solely for comparison purposes and, subsequently, to enable the use of the mechanical and viscoelastic properties in future work on the development of new devices [43]. Some parameters measured through uniaxial tensile and stress–relaxation tests were implemented in the numerical model, and the simulated response was compared with the experimental one. If the FEM successfully reproduces the observed behavior, this may confirm the validity of the simulation.

Discretization of the domain was performed by means of a 3-dimensional mesh composed of 3D solid elements of type C3D20R (i.e., 3D solid 20-node quadratic elements with reduced integration and distortion control) with an average size of 1 mm (Fig. 3(a). A mesh size sensitivity analysis was performed, until a stable, discretization-independent solution was obtained. The final mesh adopted has a higher refinement (i.e., average size of 0.5 mm) in the central area of the specimen (Fig. 3(b), where the largest strain gradients are located and where the onset of failure is observed.

For the uniaxial tensile test simulations, the boundary conditions shown in Fig. 3(c) were applied, constraining the top and bottom surfaces at both specimen side-ends. The material was assumed to be homogeneous and isotropic and was modeled using a linear elastic constitutive law. The Young's modulus and Poisson's ratio were imposed according to the experimental values obtained for each curing temperature. A time-dependent displacement control corresponding to a cross-head speed of 5 mm/min was applied in order to reproduce the experimental loading strain. The maximum elongation at break (expressed as a percentage) and UTS were extracted from the numerical simulations and compared with the corresponding experimental results.

Stress–relaxation simulations were performed using the same boundary conditions shown in Fig. 3(c). In this case, the material response was described using a Maxwell viscoelastic model, most suitable for describing viscoelastic behavior during stress–relaxation tests, with respect to other models [44]:

$$\dot{\varepsilon}_{tot} = \dot{\varepsilon}_1 + \dot{\varepsilon}_2 = \frac{\sigma}{\eta} + \frac{\dot{\sigma}}{E} \tag{6}$$

where the stress–strain behavior of the material is represented as a linear elastic spring and a viscous damper connected in series. Here, $\dot{\varepsilon}_1$ represents the strain associated with the viscous contribution, while $\dot{\varepsilon}_2$ corresponds to the one associated with the elastic contribution. This formulation captures the time-dependent stress decay under constant strain conditions and is characterized by a relaxation time constant $\tau = \eta E$, where E is the elastic modulus and η is the viscosity of the material. In the present work, the time constant τ was imposed a priori, based on experimental data results (computed as presented in Section 2.3.2).

Different initial strain levels and strain rates were imposed to reproduce the experimental loading phase. After reaching the target deformation, the strain was held constant for the entire duration of the

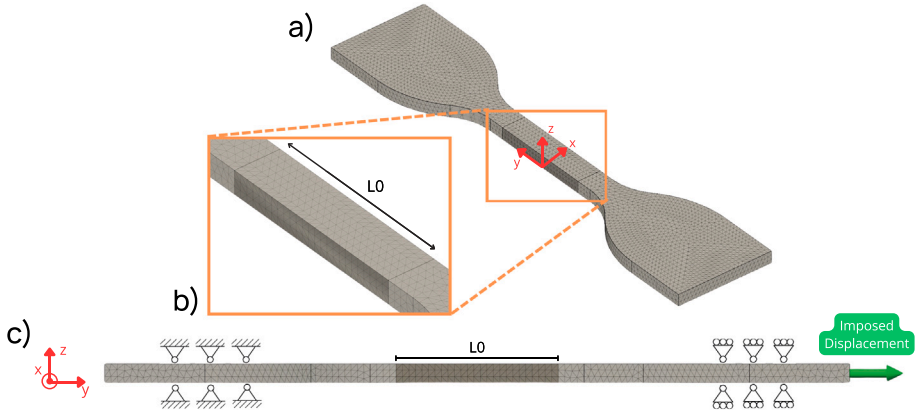

Fig. 3. Finite element model. a) Isometric view of FE model of the Dumbbell Type C specimen with 3-dimensional mesh applied. b) Zoom of the mesh on the useful zone. c) Side view of the specimen with the boundary and loading conditions applied (valid both for uniaxial and relaxation test).

simulation, in accordance with the experimental protocol. The stress–loss occurring during the holding phase was quantified from the Maxwell model response and compared with the experimentally measured relaxation behavior in order to validate the viscoelastic dissipation observed in the material.

In accordance with the experimental protocol, all simulations were performed under constant temperature conditions [45]. It is important to highlight that temperature variations associated with the curing process were not considered during the simulations, as curing was completed prior to mechanical testing. The curing temperature was imposed during specimen manufacturing and resulted in samples with different material properties, which were subsequently characterized experimentally and reproduced in the numerical simulations.

As a comparison metric, the mean absolute percentage error (i.e., MAPE) between model results and experimental test results was used as:

$$\mathrm{MAPE} = 100 \times \left| \frac{y^{\mathrm{exp}} - y^{\mathrm{FEM}}}{y^{\mathrm{exp}}} \right| \tag{7}$$

where y^{exp} represents the quantity obtained from the experimental tests (i.e., elongation, UTS or stress–loss), and y^{FEM} denotes the corresponding value predicted by the numerical model. For the uniaxial tensile tests, y^{exp} corresponds to the average value computed over the three experimental repetitions, whereas for the relaxation tests the single experimental value associated with each imposed strain level is used.

3. Results and discussion

This section presents the results obtained from experimental tensile and relaxation tests. Specifically, it discusses the mechanical properties derived from these tests, the parameters defining the material's relaxation behavior, and a comparison with the outcomes of the finite element model.

3.1. Specimens preparation: HSI analysis outcomes

The results of the HSI analysis for the presence of unconsumed reactive groups are presented in Fig. 4. Analysis of the amplitude of the first derivative of the spectrum provides direct information on the concentration of unreacted functional groups within the polymer matrix. Higher amplitude values are associated with a greater presence of unreacted groups, whereas lower values signify a greater extent of reagent consumption. Furthermore, the percentage conversion of reagents is also reported, using the first derivative of the liquid material spectrum as a reference [46]. Compared to liquid material (i.e., after being mixed and poured into the mold), those cured at 25 °C exhibit a localised increase in derivative amplitude. This suggests that, although the reaction

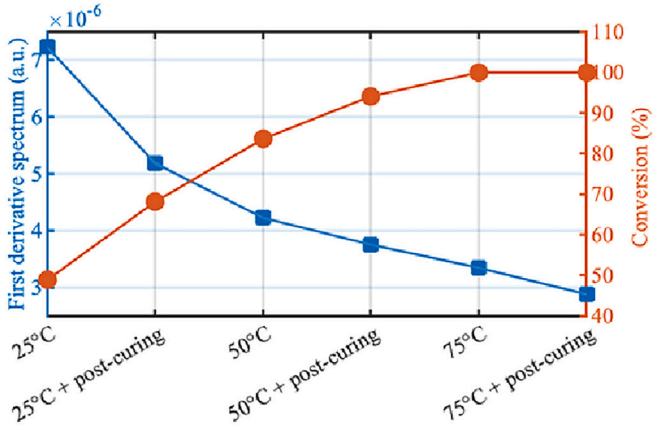

Fig. 4. Analysis of Si-H/C-H group conversion using MWIR hyperspectral imaging. The graph illustrates the first derivative of the spectrum (blue line with squares) and the percentage of conversion (orange line with circles) for each curing temperature (25°C, 50 °C and 75 °C) and condition (with and without post-curing) analyzed. (For interpretation of the references to colour in this figure legend, the reader is referred to the web version of this article).

is initiated successfully, a significant proportion of the reactive groups remain unconsumed, meaning the post-curing effect is only significant at this lower temperature. Indeed, conversion increases from 47% to approximately 70% after post-curing [47].

As the curing temperature increases to 50 °C and 75 °C, the peak-to-peak amplitude progressively decreases, indicating a more advanced reaction state and a corresponding reduction in residual Si–H group concentration. It is noteworthy that, although mathematics of the first derivative might suggest a broader range, the conversion curve is physically constrained to a 100% limit. This plateau indicates that the initial curing time is sufficient to reach full chemical maturity. Consequently, at 75 °C, the reaction completes within primary curing, taking less than 40 minutes and rendering any subsequent post-curing treatment unnecessary for further micro-structural stabilization [47,48].

3.2. Uniaxial loading tests outcomes: experimental results

The stress–strain behavior of Siliglass was assessed through uniaxial tensile loading testing, whose results revealed a profound influence of curing temperature on the mechanical properties and failure behavior of the material, as illustrated in the stress/strain curves of Fig. 5. The results (Appendix A, Table A.1), presented in Fig. 6, are reported in

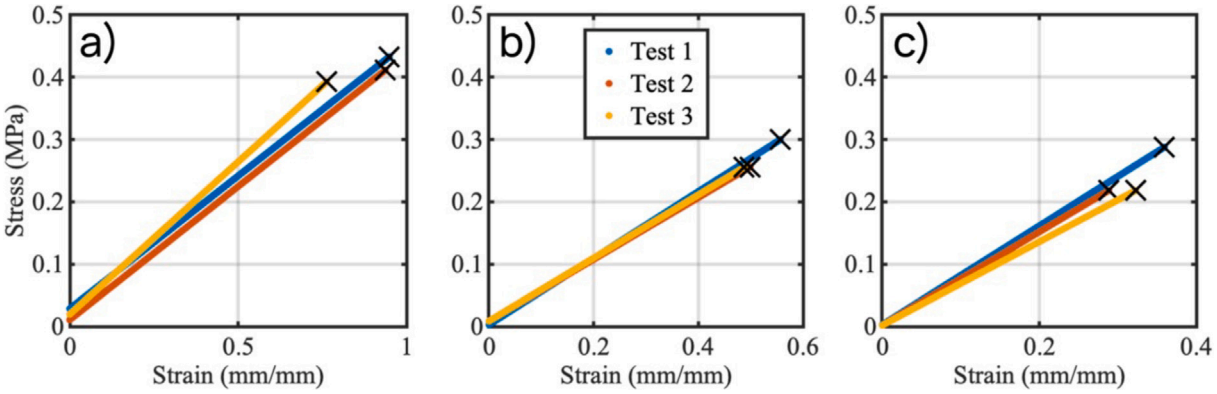

Fig. 5. Stress vs. strain curves, obtained from the experimental uniaxial loading tests, for the different curing temperatures: a) T = 25 °C. b) T = 50 °C. c) T = 75 °C. Black cross highlights the failure/rupture of the specimen. (For interpretation of the references to colour in this figure legend, the reader is referred to the web version of this article).

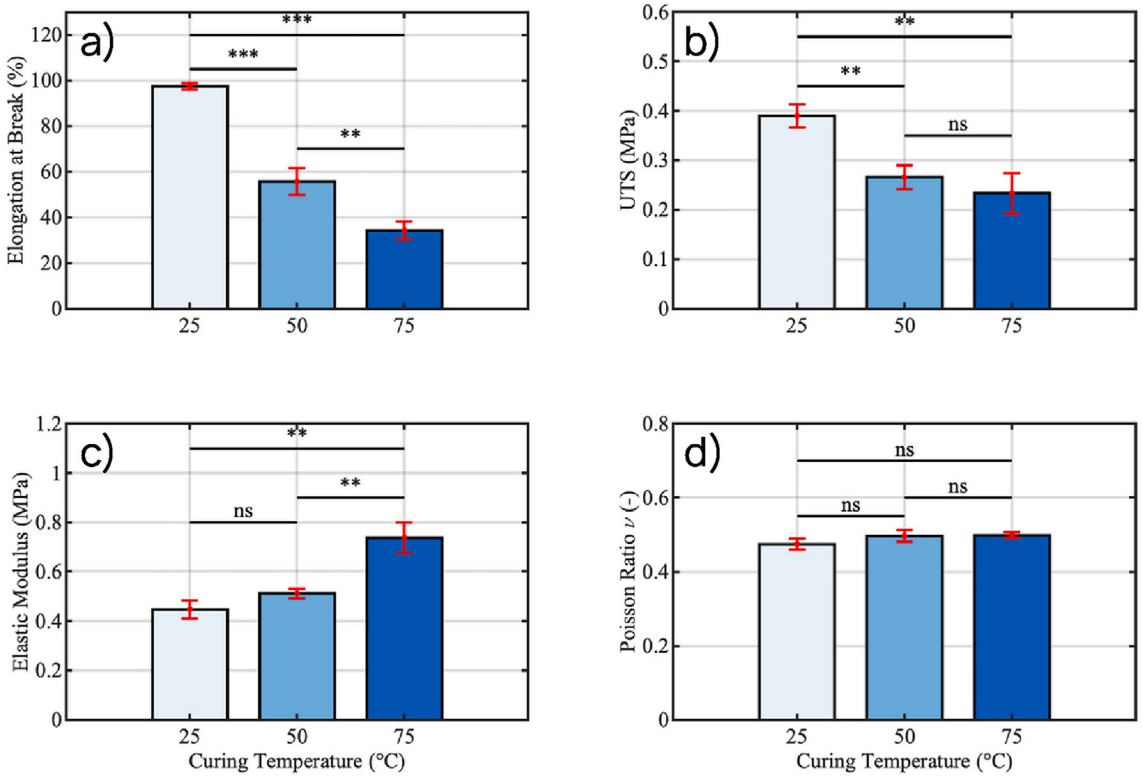

Fig. 6. Mechanical properties of Siliglass specimens obtained through uniaxial loading tests and reported for the different curing temperatures. a) elongation at break. b) UTS (i.e., Ultimate Tensile Strength). c) Young's modulus. d) Poisson's Ratio. Data are reported as mean ± standard deviation (SD, red error-bars) (n = 3). Pairwise two-sided *t*-tests were performed. Significance: $p < 0.05$ (*), $p < 0.01$ (**), $p < 0.001$ (***), *ns* = not significant. (For interpretation of the references to colour in this figure legend, the reader is referred to the web version of this article).

terms of mean value (across the three tests performed) with the standard deviation highlighted (i.e., red error bars) [49].

The most impressive remark is the drastic reduction in the material's ductility, quantified by elongation at break (Fig. 6)(a). Specimens cured at 25 °C exhibit pronounced ductile characteristics and can sustain large deformations, with an average elongation of 97 ± 2% before failure. This high degree of stretchability points to an elastic, network-like structure that can undergo extensive molecular rearrangement and chain alignment under load [50]. This behavior is similar to that of Sylgard 184, when tested under the same conditions, as provided in [51]. Curing at 50 °C, conversely, reduces this stretching capacity by half (56 ± 6%), indicating a significant reduction in molecular mobility. This trend culminates at a curing temperature of 75 °C, where elongation reaches 34 ± 4%, indicative of a predominantly brittle solid structure.

Fig. 6 thus confirms what is presented in Fig. 5: the curves for the 25 °C specimens (Fig. 6)(a) span a far greater strain axis, while the curves for 50 °C and especially 75 °C reach failure earlier than the others, recording a much smaller strain [5].

Along with the loss of ductility, a diminution in the material strength occurs as well (Fig. 6)(b). Ultimate tensile strength (UTS) decreases from 0.39 ± 0.09 MPa at 25 °C, to 0.27 ± 0.09 MPa at 50 °C, and ultimately to 0.23 ± 0.07 MPa at 75 °C. The primary mechanism driving these macroscopic changes is the degree of reagent conversion and the resulting cross-link density within the polymer matrix. This inverse relationship

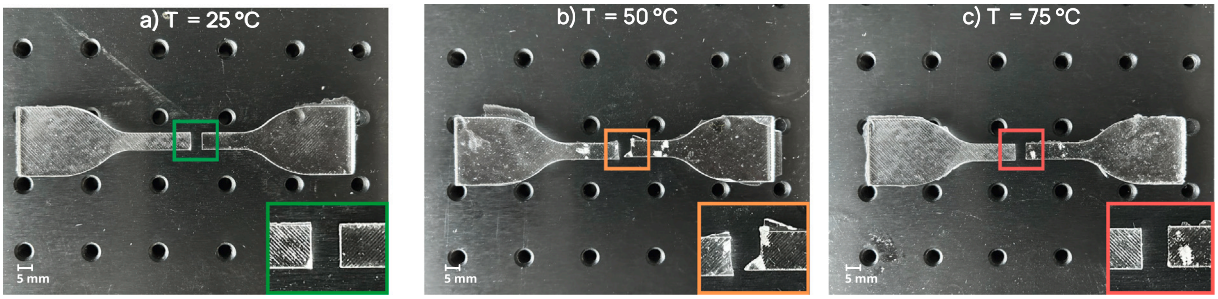

Fig. 7. Tensile fracture of specimens cured at the different temperatures: a) 25 °C. b) 50 °C. c) 75 °C. The fracture regions are marked with coloured boxes and shown in detail in the magnified insets.

between UTS and curing temperature suggests that, as the network stiffens, it also becomes more sensitive to flaws. Higher curing temperatures are likely to increase cross-link density, but the nature of these cross-links or the polymerization kinetics may result in a more heterogeneous microstructure with stress concentrators, such as microvoids or regions of uneven cross-linking [52]. Consequently, while a higher cross-link density restricts molecular slipping, thereby increasing the elastic modulus, the concurrent development of microstructural defects causes the material to fail at lower ultimate stress levels [53]. The high uncertainty values for UTS across all temperatures reflect the challenge of achieving perfect specimen homogeneity and the sensitivity of strength properties to microscopic defects [54,55].

On the other side, in contrast to the trends observed for ductility and strength, Young's modulus substantially and monotonically increases with curing temperature (Fig. 6)(c), rising from 0.45 ± 0.08 MPa at 25 °C to 0.51 ± 0.09 MPa at 50 °C and reaching 0.74 ± 0.07 MPa at 75 °C, representing an increase of over 64%. This stiffening is a classic indicator of increased cross-link density, observed also in two other elastomeric materials tested under the same conditions, namely Dragon Skin 10 and Sylgard 186 [51]: a higher curing temperature typically accelerates the curing reaction, promotes a more complete conversion, and potentially leads to a different type of cross-link (e.g., shorter and more numerous chains). All these factors contribute to a tighter, more constrained polymer network that offers greater resistance to initial elastic deformation, which aligns with the steeper initial slopes visible in the curves for the 75 °C specimens (Fig. 5)(c) [56].

Finally, the Poisson's ratio remains remarkably stable across the entire temperature range (Fig. 6)(d), in agreement with values obtained in previous studies [57]. These values are nearly 0.5 at small axial strains, which corresponds to a perfectly incompressible material, typical of rubbers and elastomers. In addition, it is possible to highlight how values of Poisson's ratio decrease as the axial strain increases (i.e., at 25 °C curing temperature elongation is the highest and Poisson's ratio the smallest), a similar trend that has also been found in [58]. The measured Poisson's ratio confirms that the Siliglass substrate cannot be considered as a volume invariant under deformation, and the accurate measurements of this parameter can help predict the performance of wearable sensor devices for human motion detection. This very similar behavior between curing temperatures in terms of Poisson's ratio also leads to an analysis of the material necking.

Fig. 7 highlights how the specimens exhibit relatively similar fracture features across all three temperatures, with sharp breaks and limited plastic deformation. This indicates a predominantly brittle failure mode. Despite the variations in stiffness and elongation at break observed in mechanical testing, the fracture morphology remains comparable, with no substantial differences in how the material ultimately fails. Particularly, at 25 °C (Fig. 7)(a), the specimen exhibits ductile failure, with significant elongation prior to rupture and smooth fracture surfaces, indicating substantial plastic deformation. When the curing temperature is increased to 50 °C (Fig. 7)(b), the material shows reduced elongation at break, accompanied by a more irregular and sharper fracture profile, characteristic of a transition from ductile to brittle-like behavior. At the highest curing temperature of 75 °C (Fig. 7)(c), the specimen fractures in a highly brittle manner, with minimal elongation and rough fracture surfaces.

These observations suggest that increasing the curing temperature enhances cross-link density or internal stresses within the polymer, thereby reducing chain mobility and leading to lower deformability [59]. Moreover, taken together, these results suggest that although an increased curing temperature can improve stiffness, as indicated by the elastic modulus, it reduces ductility, as demonstrated by the decreased elongation at break. The Poisson's ratio appears to be less sensitive to curing conditions, as also confirmed by small necking and fracture final shape.

3.3. Uniaxial relaxation tests outcomes: experimental results

The stress–relaxation behavior of Siliglass was studied through uniaxial relaxation tests, firstly by imposing different initial strains, in terms of displacement (i.e., mm). Fig. 8 shows the temporal evolution of the relaxation ratio (RR) for the three different curing temperatures and for three different displacement levels (i.e., 2.5 mm, 5 mm, and 7.5 mm). In all cases, the RR exhibits rapid decrease at the beginning of the holding phase and declines gradually as the holding time progresses. Generally, Siliglass does not show significant relaxation, like other elastomeric materials (e.g., natural rubber) [60] and polymeric ones [61]. However, both the rate and the extent of this decrease are strongly affected by temperature and initial strain.

The influence of imposed displacement is evident across all the three graphs. For a given temperature, higher imposed displacements (5 mm and 7.5 mm) generally result in consistently lower RR values throughout the test. This suggests that larger initial deformations induce higher internal stresses, which in turn promote greater relaxation. An exception is observed at the curing temperature of 50 °C, where all the RR values exhibit similar behavior over time. It can be seen, in addition, that most of the relaxation happens at the beginning (less than 200 s) of the holding phase, and the specimens under higher imposed strain take more time to reach steady state condition: an example can be appreciated in Fig. 8(a), where the specimen stretched at 7.5 mm does not fully reach this condition [62].

As another factor affecting the relaxation of Siliglass cured at different temperatures, the impact of strain speed is also investigated by stretching the specimens at different initial imposed strain speeds, in terms of displacement per unit time (i.e., mm/s). In Fig. 9 temporal evolutions of relaxation ratio for the three different curing temperatures are presented for the three different values of strain speed applied (i.e., 0.5 mm, 1.5 mm, and 2.5 mm), showing very similar relaxation trends and behavior with respect to tensioning the specimens with different initial displacements. By comparing the RR, it is observed that more

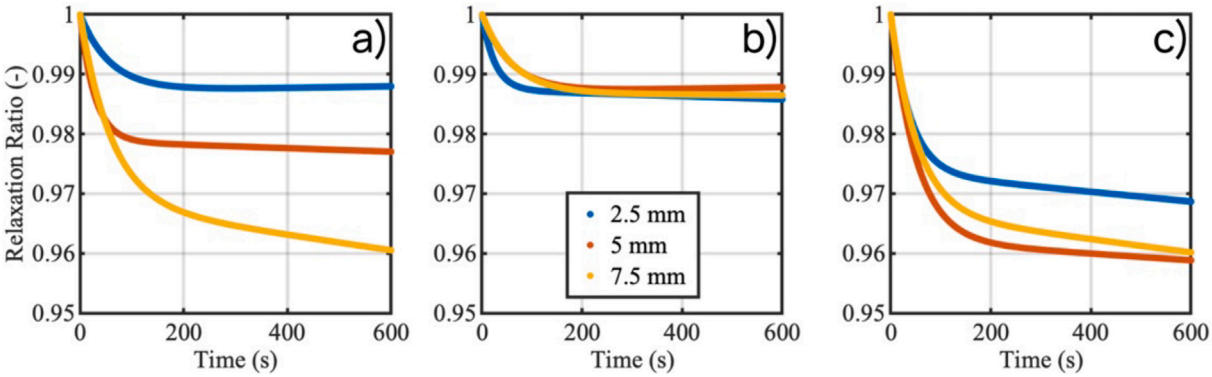

Fig. 8. Relaxation ratio (RR) obtained from the experimental uniaxial relaxation tests, for the different curing temperatures: a) T = 25 °C. b) T = 50 °C. c) T = 75 °C and for different initial imposed strain (in mm, according to the legend).

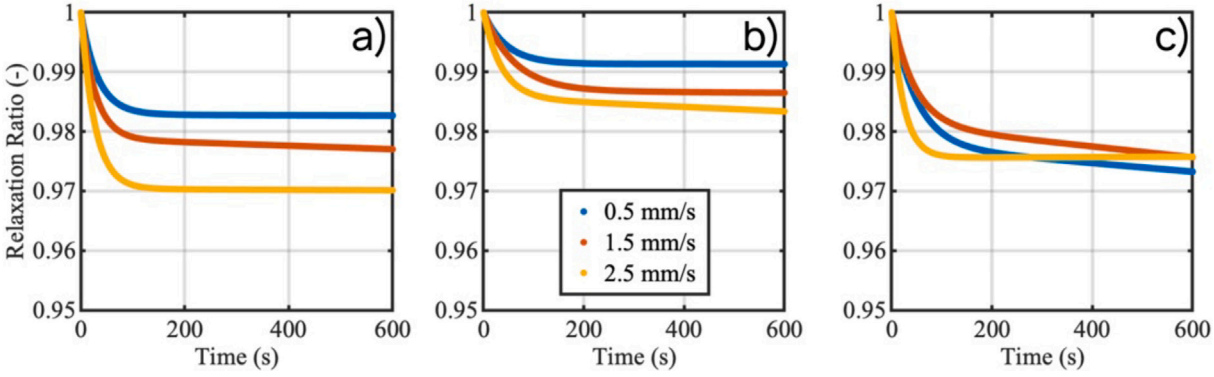

Fig. 9. Relaxation ratio (RR) obtained from the experimental uniaxial relaxation tests, for the different curing temperatures: a) T = 25 °C. b) T = 50 °C. c) T = 75 °C and for different initial imposed strain speed (in mm/s, according to the legend).

relaxation occurs with increasing the strain speed (i.e., increasing stress–loss as speed increases), which can be explained by unevenly distributed stress in deforming the specimens under different and rising strain rates. Most of the relaxation occurs, also here, in the beginning (first 200 s), reaching a fully steady state at 25 °C for all three imposed strain speeds (Fig. 9)(a). Such behavior is very similar in terms of RR for all strain rates when curing is performed at 75 °C (Fig. 9)(c). The behavior at 50 °C remains unchanged in terms of relaxation obtained (i.e., stress–loss) between the two testing conditions (Figs. 8)(b) and 9(b).

These initial results are further confirmed by the loss values, calculated as described above and shown in Figs. 10(a) and Fig. 11(a).

When an initial strain is imposed (Fig. 11)(a), it can be observed that the stress–loss values at curing temperatures of 25 °C and 75 °C are higher than those of specimens cured at 50 °C. Moreover, the specimen cured at 25 °C shows an increasing trend in stress–loss, reaching a maximum of 4% as the initially imposed strain increases. This pronounced viscoelastic response is directly governed by the lower cross-link density achieved at 25 °C, which preserves a higher segmental mobility of the polymer chains. Under rising initial strains, these unconstrained segments can undergo extensive physical rearrangement, translating into a greater capacity for energy dissipation and stress–loss [63]. This behavior is not observed for specimens cured at 50 °C and 75 °C where the tightly cross-linked network structurally restricts such long-range segmental motions, and it is consistent with the relaxation ratio (RR) trends shown in Figs. 8 and 9.

The increasing trend in stress–loss for the sample cured at 25 °C is also visible in Fig. 10(a), when the strain rate is increased, although in this case the maximum stress–loss is slightly lower (around 3%). A similar trend can be noted for the specimen cured at 50 °C, but it is less pronounced, as indicated by the gentler slope of the curve. In contrast, for the specimen cured at 75 °C, the stress–loss remains approximately constant (Fig. 9)(c).

Finally, the overlap of curves (Fig. 8)(b) and the similarity in stress–loss values (Fig. 9)(a) for the 50 °C curing temperature suggest the existence of a transition region between temperature-dominated and strain-dominated regimes. Overall, the observed stress–loss values are comparable to those previously reported for thermoplastic polymers and elastomers [64].

To fully evaluate the relaxation behavior of the material, the time constant values were computed and are reported in Figs. 10(b) and Fig. 11(b). Considering the different initial strains (Fig. 11)(b), a general increasing trend of the time constant with increasing imposed strain is observed for all curing temperatures. This behavior, visible from the slope of each individual curve, is more pronounced for the specimen cured at 25 °C and gradually decreases as the curing temperature increases. This indicates a stronger viscoelastic effect when the material is cured near room temperature and, in general, under higher initial deformations. The highest time constant values for this case are 60.89 s and 61.42 s (for T = 25 °C and T = 50 °C, respectively, see Appendix A), both corresponding to an initial strain of 7.5 mm.

On the other hand, when different initial strain rates are applied, Fig. 11(b) shows a clear decrease in the time constant as the strain rate increases. This trend, also reported in [65], indicates that the material relaxes faster under higher deformation rates. A plausible explanation is that at higher strain speeds, the microstructural rearrangements responsible for stress–relaxation are more easily activated, resulting in a shorter characteristic relaxation time.

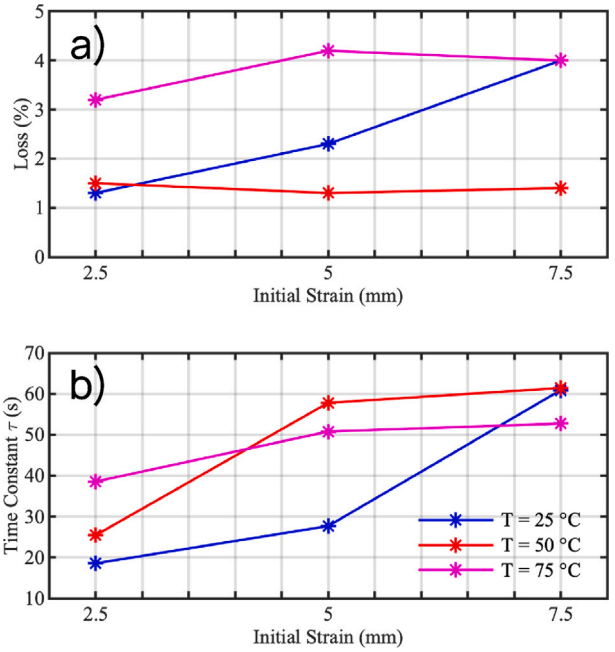

Fig. 10. Stress–loss (a) and time constant (b) resulting from uniaxial relaxation tests, for different initial imposed strains (in mm) and for the different curing temperatures (according to the legend). Numerical values are reported in Appendix A, Table A.2.

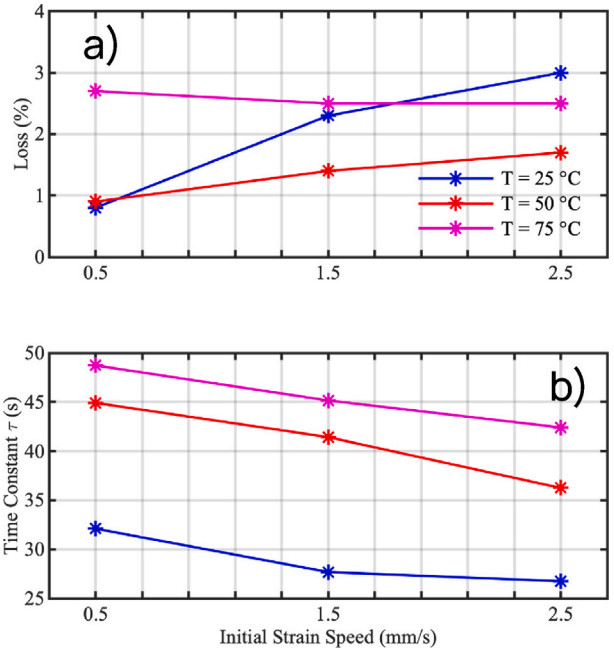

Fig. 11. Stress–loss (a) and time constant (b) resulting from uniaxial relaxation tests, for different initial imposed strain speeds (in mm/s) and for the different curing temperatures (according to the legend). Numerical values are reported in Appendix A, Table A.3.

Additionally, the systematic offset between the curves suggests that intrinsic material parameters, such as composition, cross-link density, or molecular mobility, significantly influence the absolute magnitude of the time constant [66]. At 75 °C, the higher degree of reagent conversion promotes a tighter network with short, highly dense cross-links. This configuration drastically bounds the segmental mobility, forcing the relaxation to rely on highly-constrained, local molecular cooperative movements that demand higher activation energy and result in higher time constants at low strain rates. In this case, contrary to the previous scenario, the highest time constant is observed at a strain rate of 0.5 mm/s for the specimen cured at 75 °C. Conversely, the open and flexible matrix of the 25 °C cured specimens alters this relaxation spectrum due to the free chain dynamics. Overall, the analysis confirms the trends observed in the relaxation ratio (Fig. 9), providing a consistent picture of the material's viscoelastic behavior.

3.4. Uniaxial and relaxation loading tests outcomes: comparison with FEM

As anticipated, a comprehensive numerical analysis was carried out through the development of a dedicated finite element (FEM) model to support the interpretation of the experimental uniaxial tensile and relaxation tests. The objective was to evaluate the capability of the model to reproduce the mechanical response of the material and to quantify the agreement between numerical results and experimental measurements across the three curing temperatures investigated.

The comparative results for the tensile tests are reported in Fig. 12, which show the evolution of elongation at break and UTS with curing temperature for both experiments and FEM simulations.

Fig. 12(a) presents the elongation at break. Both datasets show a clear decrease in ductility as the curing temperature increases, in agreement with the trend previously highlighted in Fig. 6. The FEM model successfully captures this behavior, reproducing the experimental curves with good overall accuracy. As expected, the mean absolute percentage error (MAPE) increases with curing temperature, reflecting the greater difficulty in replicating the more brittle response associated with higher cross-link densities. Nevertheless, MAPE values remain below 12% for

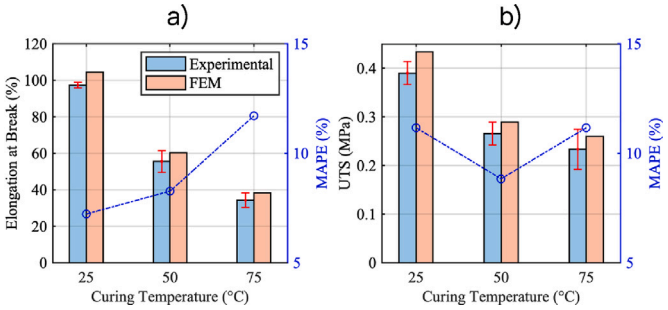

Fig. 12. Comparison between experimental results of uniaxial tensile tests (blue bars) and FEM analysis (orange bars) for specimens cured at 25 °C, 50 °C, and 75 °C. a) Elongation at break (%). b) Ultimate tensile strength (i.e., UTS, MPa). Experimental data are reported as mean ± standard deviation (SD, red error-bars) (n = 3). Mean absolute percentage error (MAPE, %) is reported for both the outputs (i.e., blue dashed line). (For interpretation of the references to colour in this figure legend, the reader is referred to the web version of this article).

all cases, with only slightly larger discrepancies observed for specimens cured at 75 °C. These results demonstrate the reliability of the numerical approach in predicting the experimentally observed reduction in ductility.

Fig. 12(b) shows the evolution of the UTS with curing temperature. A moderate decrease in strength is observed as the curing temperature increases, which can be attributed to reduced polymer-chain mobility and the corresponding decrease in fracture toughness due to higher cross-linking. The FEM predictions capture the experimental trend well, with MAPE values slightly above 10% for specimens cured at 25 °C and 75 °C. Despite these minor deviations, the strong agreement between simulations and experiments demonstrates the robustness of the model in predicting the temperature-dependent reduction in strength.

Fig. 13 enhances the tensile-test analysis by comparing the experimental and FEM-predicted stress–loss (%) during relaxation tests at the three curing temperatures. For each curing condition, the left

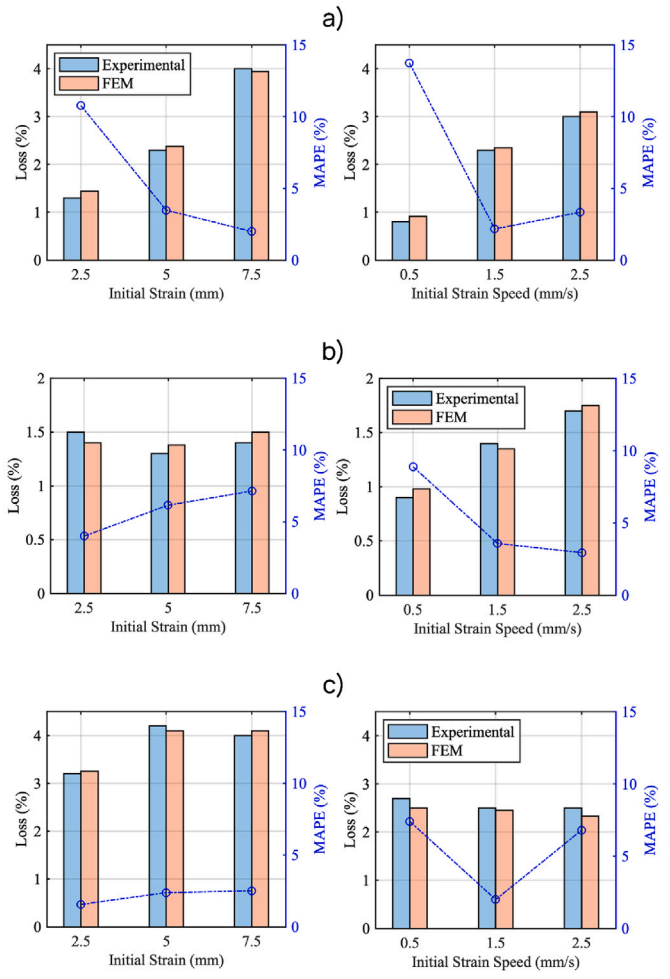

Fig. 13. Comparison between experimental results (blue bars) and FEM analysis (orange bars) of stress–loss (%), occurring during relaxation tests, for the three curing temperatures: a) T = 25 °C. b) T = 50 °C. c) T = 75 °C. For each curing condition: (left) stress–loss as a function of the imposed initial strain. (right) stress–loss as a function of the initial strain rate. The superimposed line (i.e, blue dashed) represents the mean absolute percentage error (MAPE, %). (For interpretation of the references to colour in this figure legend, the reader is referred to the web version of this article).

panels show stress–loss as a function of the imposed initial strain, while the right panels show stress–loss as a function of the initial strain rate. The superimposed dashed line indicates the corresponding MAPE.

Across all curing temperatures, FEM simulations reproduce the experimental stress–relaxation behavior with good accuracy. At T = 25 °C (Fig. 13)(a), both strain-dependent and rate-dependent trends are well captured, with MAPE values consistently below 10%. At T = 50 °C (Fig. 13)(b), numerical results remain in close agreement with experiments, even as the stress–loss response becomes slightly less sensitive to initial strain. MAPE remains low and shows only modest variation with strain or strain rate. For specimens cured at T = 75 °C (Fig. 13)(c), higher stress–loss is observed experimentally, consistent with increased brittleness and reduced molecular mobility due to a higher degree of cure. The FEM model successfully reproduces this behavior, although MAPE values show a slight increase, similar to what was observed for the tensile properties at the same curing temperature. Nevertheless, the numerical predictions closely follow the experimental trends, confirming the robustness of the viscoelastic model.

Overall, the comparison between experimental measurements and FEM simulations demonstrates that the proposed numerical framework accurately supports the experimental results, both for the tensile response and the time-dependent relaxation behavior of the material across all curing temperatures. The consistently low MAPE, which remains below approximately 12%, further confirms the reliability of the modeling approach and reinforces the validity of the experimental observations.

It is important to note that the viscoelastic behavior of Siliglass platinum-cured silicone after cross-linking can be effectively described in terms of an *effective viscosity*, calculated as the product of the material's elastic modulus and its characteristic relaxation time [67]. In our study, with an average modulus of approximately 0.45 MPa and a relaxation time of 27.5 s across the curing temperatures, the resulting effective viscosity is on the order of 10^7 Pa·s. This represents an increase of several orders of magnitude compared to the pre-cure liquid state (0.2 Pa·s), reflecting the transition from a low-viscosity fluid to a cross-linked elastomer [67,68]. While the material behaves essentially as a solid over typical observation times, the finite relaxation time highlights its viscoelastic nature, allowing for stress–relaxation under long-term loading [69].

4. Conclusion

The influence of curing temperature on the mechanical and stress–relaxation properties of Siliglass platinum silicone was analyzed in this work, with the aim of evaluating its suitability for wearable strain sensors and optical phantoms. The results showed that the curing temperature significantly impacts ductility, tensile strength, and stiffness. Specimens cured at 25 °C exhibited high stretchability, making this combination of temperature and time of curing an eligible protocol to create tissue-like viscoelastic phantoms, while those cured at 75 °C displayed brittle behavior and a higher modulus. Although Poisson's ratio remained nearly constant, confirming the incompressibility of such material, slight variations with strain highlight the need for an accurate characterization.

In comparison with state-of-the-art research on flexible elastomers, this study demonstrates that Siliglass offers superior tunability; while many standard silicones exhibit fixed mechanical profiles, the curing protocols identified here allow for a modulation of properties to match specific requirements. These findings provide a comprehensive understanding of how curing temperature regulates the macro-scale response of the polymer. Stress–relaxation tests demonstrated that curing temperature and loading conditions impact the viscoelastic response; faster relaxation was observed at higher strain rates. A finite element model was implemented to better interpret the experimental data, effectively supporting the reliability of the approach adopted, and represents a tool for the design and optimization of smart wearable monitoring systems.

Overall, Siliglass exhibits tunable properties through curing conditions, making it versatile for different applications. This work contributes by bridging the gap between polymer processing parameters and functional performance in soft electronics. These insights provide valuable guidelines for optimizing Siliglass for use in advanced flexible and wearable technologies, highlighting its potential as a benchmark material for these applications.

Future developments will focus on complementary tests, such as compression and cyclic loading, as well as integrating embedded sensors to enable in situ monitoring and enhance functional performance. Additional directions include the realization of optical phantoms and the measurement of optical properties at different curing temperatures. Moreover, the adoption of alternative and more detailed viscoelastic models will be explored, integrating the effects of environmental factors and ageing, particularly in cases where a deeper understanding of the material behavior is of interest for the specific application.

CRediT authorship contribution statement

L. Maggioni: Writing – original draft, Visualization, Validation, Software, Methodology, Investigation, Data curation, Conceptualization.

E. Lacagnina: Writing – original draft, Visualization, Validation, Investigation, Data curation, Conceptualization. **A. Cigada:** Writing – review & editing, Supervision. **P. Saccomandi:** Writing – review & editing, Supervision, Funding acquisition, Conceptualization.

Declaration of competing interest

The authors declare that they have no known competing financial interests or personal relationships that could have appeared to influence the work reported in this paper.

Acknowledgements

This work has received funding from the European Union - NextGenerationEU, M4C2 I1.1, Project PRIN 2022 "ARTIS", Prot. 20228H4ZR3, CUP D53D23001080006, and from the European Research Council (ERC) under the European Union's Horizon Europe research and innovation programme (Grant Agreement No. 101212894). The authors would also like to thank Ing. Marco Papetti for his assistance and support with the experimental work and data analysis related to the hyperspectral imaging measurements (Sections 2.1 and 3.1).

Appendix A. Numerical results of experimental tests

Table A.1
Mechanical properties at different curing temperatures (mean ± standard deviation).

	Curing temperature (°C)		
	25	50	75
Elongation at break (%)	97 ± 2	56 ± 6	34 ± 4
UTS (MPa)	0.39 ± 0.09	0.27 ± 0.09	0.23 ± 0.07
Young's modulus (MPa)	0.45 ± 0.08	0.51 ± 0.05	0.74 ± 0.07
Poisson ratio ν	0.47 ± 0.05	0.49 ± 0.06	0.50 ± 0.03

Table A.2
Stress–loss (%) values obtained from the uniaxial relaxation tests.

	Curing temperature (°C)		
Initial imposed strain (mm)	25	50	75
2.5	1.30	2.30	4.00
5.0	1.50	1.30	1.40
7.5	3.20	4.20	4.00
Initial imposed strain speed (mm/s)	25	50	75
0.5	0.80	2.30	3.00
1.5	0.90	1.40	1.70
2.5	2.70	2.50	2.50

Table A.3
Time constant τ (s) values obtained from the uniaxial relaxation tests.

	Curing temperature (°C)		
Initial imposed strain (mm)	25	50	75
2.5	18.55	27.68	60.89
5.0	25.43	27.59	61.42
7.5	38.56	50.78	52.70
Initial imposed strain speed (mm/s)	25	50	75
0.5	32.10	27.68	26.74
1.5	44.90	41.42	36.25
2.5	44.72	45.15	42.40

Data availability

Data will be made available on request.

References

[1] E. Teixeira, H. Fonseca, F. Diniz-Sousa, L. Veras, G. Boppre, J. Oliveira, D. Pinto, A.J. Alves, A. Barbosa, R. Mendes, I. Marques-Aleixo, Wearable devices for physical activity and healthcare monitoring in elderly people: a critical review, Geriatrics 6 (2) (2021), https://doi.org/10.3390/geriatrics6020038
[2] M.A. Abdelfattah, S.S. Jamali, N. Kashaninejad, N.-T. Nguyen, Wearable biosensors for health monitoring: advances in graphene-based technologies, Nanoscale Horiz. 10 (8) (2025) 1542–1574.
[3] V. Kumar, N. Parvin, S.W. Joo, T.K. Mandal, S.S. Park, Great carbon nano materials based composites for electronic skin: intelligent sensing, and self-powered nano generators, Nano Energy 137 (2025) 110805.
[4] V. Kumar, M.N. Alam, M.A. Yewale, S.S. Park, Great elastomer-based composites for robust and portable wearable sensors: a critical review, Sens. Actuators a Phys. 389 (2025) 116563.
[5] X. Fang, J. Tan, Y. Gao, Y. Lu, F. Xuan, High-performance wearable strain sensors based on fragmented carbonized melamine sponges for human motion detection, Nanoscale 9 (45) (2017) 17948–17956.
[6] J. Chen, Y. Zhu, W. Jiang, A stretchable and transparent strain sensor based on sandwich-like PDMS/CNTs/PDMS composite containing an ultrathin conductive CNT layer, Compos. Sci. Technol. 186 (2020) 107938.
[7] D. Paloschi, L. Maggioni, L. Airoldi, G. Alaimo, C. Boselli, L. D'Antoni, P. Saccomandi, Fiber optic-based wearable sensing device for foot curvature monitoring in classic ballet dancing, in: 2024 IEEE International Symposium on Medical Measurements and Applications (MeMeA), IEEE, 2024, pp. 1–6.
[8] M. Fajkus, J. Nedoma, P. Siska, V. Vasinek, FBG sensor of breathing encapsulated into polydimethylsiloxane, in: Optical Materials and Biomaterials in Security and Defence Systems Technology XIII, 9994, 2016, p. 99940N. https://doi.org/10.1117/12.2241663
[9] H. Souri, et al., Wearable and stretchable strain sensors: materials, sensing mechanisms, and applications, Adv. Intell. Syst. 2 (8) (2020) 2000039, https://doi.org/10.1002/aisy.202000039
[10] Y.A. Samad, Y. Li, A. Schiffer, S.M. Alhassan, K. Liao, Graphene foam developed with a novel two-step technique for low and high strains and pressure-sensing applications, Small 11 (20) (2015) 2380–2385, https://doi.org/10.1002/smll.201403532
[11] D. Krizan, J. Stipal, M. Fajkus, J. Bohacova, A. Leal-Junior, C. Marques, J. Nedoma, Analysis of different integration approaches of fiber bragg gratings into wearable textiles for sensing of vital signs, Measurement (2025) 118164.
[12] L. Maggioni, S. Del Chicca, D. Paloschi, L. Bianchi, A. Cigada, P. Saccomandi, Design and fabrication of fiber bragg gratings-based flexible insole for monitoring execution of classical dance exercises, IEEE Sens. J. 25 (11) (2025) 19242–19249.
[13] X. Song, Y. Fan, X. Tang, FBG-based wearable sensors and devices in the healthcare field: a review, Opt. Laser Technol. 181 (2025) 111920.
[14] K. Xiao, Z. Wang, Y. Ye, C. Teng, R. Min, PDMS-embedded wearable FBG sensors for gesture recognition and communication assistance, Biomed. Opt. Express 15 (3) (2024) 1892–1909.
[15] F. Velazquez-Carreon, A. Perez-Alonzo, G. Sandoval-Romero, C. Sanchez-Perez, Enhanced PDMS-embedded FBG devices for displacement sensing, Opt. Laser Technol. 179 (2024) 111269.
[16] E. Cho, L.L.Y. Chiu, M. Lee, D. Naila, S. Sadanand, S.D. Waldman, D. Sussman, Characterization of mechanical and dielectric properties of silicone rubber, Polymers 13 (11) (2021) 1831.
[17] K. Khanafer, A. Duprey, M. Schlicht, R. Berguer, Effects of strain rate, mixing ratio, and stress-strain definition on the mechanical behavior of the polydimethylsiloxane (PDMS) material as related to its biological application, Biomed. Microdevices 11 (2009) 503–508.
[18] M. Liu, J. Sun, Q. Chen, Influences of heating temperature on mechanical properties of polydimethylsiloxane, Sens. Actuators A 151 (1) (2009) 42–45.
[19] T. Rey, G. Chagnon, J.-B. Le Cam, D. Favier, Influence of the temperature on the mechanical behaviour of filled and unfilled silicone rubbers, Polym. Test. 32 (3) (2013) 492–501.
[20] R. Moučka, M. Sedlačík, J. Osička, et al., Mechanical properties of bulk sylgard 184 and its extension with silicone oil, Sci. Rep. 11 (2021) 19090.
[21] T.K. Kim, J.K. Kim, O.C. Jeong, Measurement of nonlinear mechanical properties of PDMS elastomer, Microelectron. Eng. 88 (8) (2011) 1982–1985.
[22] Y. Gunay, C. Kurtoglu, A. Atay, B. Karayazgan, C.C. Gurbuz, Effect of Tulle on mechanical properties of maxillofacial silicone elastomer, Dent. Mater. J. 27 (6) (2008) 775–779.
[23] A. Victor, J. Ribeiro, F.F. Araújo, Study of PDMS characterization and its applications in biomedicine: a review, J. Mech. Eng. Biomech. 4 (1) (2019) 1–9.
[24] J.B. Pascual-Francisco, L.I. Farfan-Cabrera, O. Susarrey-Huerta, Characterization of tension set behavior of a silicone rubber at different temperatures via digital image correlation, Polym. Test. 81 (2020) 106226.
[25] W. Zhang, B. Yin, J. Wang, A. Mohamed, H. Jia, Ultrasensitive and wearable strain sensors based on natural rubber/graphene foam, J. Alloys Compd. 785 (2019) 1001–1008.
[26] Polytek Development Corp., Platsil® 71 and 73-Series Silicone Rubbers, Technical Bulletin, Easton, PA, USA, 2025.
[27] ASTM D412-16R21: Standard Test Methods for Vulcanized Rubber and Thermoplastic Elastomers—Tension, 2021, https://doi.org/10.1520/D0412-16R21
[28] R. Hopf, L. Bernardi, J. Menze, M. Zündel, E. Mazza, A.E. Ehret, Experimental and theoretical analyses of the age-dependent large-strain behavior of sylgard 184 (10:1) silicone elastomer, J. Mech. Behav. Biomed. Mater. 60 (2016) 425–437.

[29] H.R. Kricheldorf, O. Nuyken, G. Swift, Handbook of Polymer Synthesis, CRC Press, 2004.
[30] O. Vryonis, T. Andritsch, A. Vaughan, P. Morshuis, A. Claverie, On the post-curing thermal treatment of silicone rubbers: a study on electrical performance, J. Appl. Polym. Sci. 142 (34) (2025) e57358.
[31] E.-B. Brăilă, V.T. Alexa, S. Dinu, V. Bolchis, V. Titus, V. Gabriela, A. Galuscan, D. Jumanca, Structural stability of silicone-based elastodontic appliances after clinical use: insights from FTIR spectroscopy, Materials 19 (1) (2025) 13.
[32] D. Paloschi, A. Polimadei, et al., Fiber bragg gratings embedded inside 3D-printed patches, in: 2023 IEEE International Workshop on Metrology for Living Environment, 2023, pp. 45–49.
[33] ASTM E132-17R25E01: Standard Test Method for Poisson's Ratio at Room Temperature, 2025, https://doi.org/10.1520/E0132-17R25E01
[34] S. Saseendran, M. Wysocki, J. Varna, Cure-state dependent viscoelastic poisson's ratio of LY5052 epoxy resin, Adv. Manuf.: Polym. Compos. Sci. 3 (3) (2017) 92–100.
[35] J.A. Sotomayor-Del Moral, J.B. Pascual-Francisco, O. Susarrey-Huerta, C.D. Resendiz-Calderon, E.A. Gallardo-Hernández, L.I. Farfan-Cabrera, Characterization of viscoelastic poisson's ratio of engineering elastomers via DIC-based creep testing, Polymers 14 (9) (2022) 1837.
[36] X. Chen, L. Falzon, J. Zhang, X. Zhang, R.-Q. Wang, K. Du, Experimental and theoretical study on the microparticle trapping and release in a deformable nano-sieve channel, Nanotechnology 31 (5) (2019) 05LT01.
[37] N. Hayeemasae, A. Adair, A. Masa, Comparative study on viscosities, stress relaxation, curing and mechanical properties of sepiolite and silica filled natural rubber composites, Malays. J. Anal. Sci 26 (2022) 176–190.
[38] ASTM E328-26: Standard Test Methods for Stress Relaxation for Materials and Structures, 2026, https://doi.org/10.1520/E0328-26
[39] Z. Liu, K. Yeung, The preconditioning and stress relaxation of skin tissue, J. Biomed. Pharm. Eng. 1 (1) (2008) 22–28.
[40] S. Zhang, C. Ge, R. Liu, Mechanical characterization of PDMS substrate for wearable strain sensors under uniaxial loading, Sens. Actuators A 341 (2022) 113580.
[41] P. Hajikarimi, F. Moghadas Nejad, Mechanical models of viscoelasticity, in: Applications of Viscoelasticity: Bituminous Materials Characterization and Modeling, Elsevier, Amsterdam, 2021, pp. 27–41, https://doi.org/10.1016/B978-0-12-821210-3.00003-6
[42] H.J. Qi, M.C. Boyce, Stress-strain behavior of thermoplastic polyurethanes, Mech. Mater. 37 (8) (2005) 817–839.
[43] N.A. Zulkifli, G.D. Moon, D.C. Hyun, S. Lee, Comprehensive constitutive modeling and analysis of multi-elastic polydimethylsiloxane (PDMS) for wearable device simulations, Sci. Rep. 13 (1) (2023) 18413.
[44] X. Zhou, D. Yu, O. Barrera, Mechanics constitutive models for viscoelastic solid materials: development and a critical review, Adv. Appl. Mech. 56 (2023) 189–321.
[45] D. SIMULIA, Abaqus 2025 Documentation Manual, Dassault Systèmes Simulia Corp., Version 2025 Edition, Manuale ufficiale del software Abaqus, disponibile in formato HTML/PDF 2025, https://2025.help.altair.com/.
[46] M. Kwaśny, A. Bombalska, K. Obroniecka, A reliable method of measuring the conversion degrees of methacrylate dental resins, Sensors 22 (6) (2022) 2170.
[47] T.S. Vo, T.S. Nguyen, B. Jeon, T.T.B.C. Vo, S. Han, S.-H. Lee, K. Kim, Characteristics and preliminary healing ability of polydimethylsiloxane elastomers, J. Mater. Res. Technol. 37 (2025) 2378–2392.
[48] C. Nedelcu, F.B. Madsen, A.L. Skov, Tunable silicone elastomers through PDMS ring network design and post-curing chemistry, Polym. Chem. 17 (13) (2026) 1278–1290.
[49] Joint Committee for Guides in Metrology (JCGM), Guide to the Expression of Uncertainty in Measurement — Part 1: Introduction, 2023, https://doi.org/10.59161/JCGMGUM-1-2023
[50] O. Guney, E. Demirkesen, Influence of curing conditions on the mechanical properties of silica-phenolic composites: a comprehensive study, Int. Adv. Res. J. Sci. Eng. Technol. 2 (11) (2015).
[51] S. Park, K. Mondal, R.M. Treadway, V. Kumar, S. Ma, J.D. Holbery, M.D. Dickey, Silicones for stretchable and durable soft devices: beyond Sylgard-184, ACS Appl. Mater. Interfaces 10 (13) (2018) 11261–11268.
[52] J. Huang, P. Fu, W. Li, L. Xiao, J. Chen, X. Nie, Influence of crosslinking density on the mechanical and thermal properties of plant oil-based epoxy resin, RSC Adv. 12 (36) (2022) 23048–23056.
[53] J.E. Mark, B. Erman, M. Roland, The Science and Technology of Rubber, Academic Press, 2013.
[54] L. Feng, S. Li, S. Feng, Preparation and characterization of silicone rubber with high modulus via tension spring-type crosslinking, RSC Adv. 7 (22) (2017) 13130–13137.
[55] S. Jiang, Z. Yong, Modulation of mechanical properties of silica-filled silicone rubber by cross-linked network structure, Polymers 16 (16) (2024) 2304.
[56] Y. Konku-Asase, A. Yaya, K. Kan-Dapaah, Curing temperature effects on tensile properties of $\gamma - Fe_2O_3$ reinforced PDMS nanocomposites, Adv. Mater. Sci. Eng. 2020 (2020) 6562373.
[57] H.S. Kang, S. Kim, H. Song, Y. Lee, J. Jang, W.G. Chung, C.-Y. Gu, J. Kim, T.-S. Kim, S. Ryu, et al., Skin-tailored adhesive bio-electrode with tunable poisson's ratio for stable electrophysiological communication, Adv. Healthc. Mater. 14 (10) (2025) 2404882.
[58] A. Müller, M.C. Wapler, U. Wallrabe, A quick and accurate method to determine the poisson's ratio and the coefficient of thermal expansion of PDMS, Soft Matter 15 (4) (2019) 779–784.
[59] C. Lou, E. Liu, T. Cheng, et al., Highly stretchable and self-adhesive elastomers for high-performance strain sensors, ACS Omega 7 (7) (2022) 5825–5835.
[60] X. Zheng, B. Li, Study on sealing performance of packer rubber based on stress relaxation experiment, Eng. Fail. Anal. 129 (2021) 105692.
[61] D. Paloschi, A. Polimadei, S. Korganbayev, V. Orsetti, C. Mazzotta, A. Cigada, M.A. Caponero, P. Saccomandi, Three-dimensional-printed sensing samples embedding fiber bragg gratings: metrological evaluation of different sample materials and fiber coatings, IEEE Trans. Instrum. Meas. 72 (2023) 1–10.
[62] L. Maggioni, D. Paloschi, V. Orsetti, A. Cigada, M. Caponero, P. Saccomandi, Characterization of hysteretic mechanical behavior of fiber bragg gratings-based curvature sensors for biomechanical applications, in: 2025 IEEE Medical Measurements & Applications (MeMeA), IEEE, 2025, pp. 1–6.
[63] L.H. Sperling, Interpenetrating Polymer Networks and Related Materials, Springer Science & Business Media, 2012.
[64] I.L. Bundalo, K. Nielsen, G. Woyessa, O. Bang, Long-term strain response of polymer optical fiber FBG sensors, Opt. Mater. Express 7 (3) (2017) 967–976.
[65] Y.-S. Jhao, H. Ouyang, F. Yang, S. Lee, Thermo-mechanical and creep behaviour of polylactic acid/thermoplastic polyurethane blends, Polymers 14 (23) (2022) 5276.
[66] J. Zhao, P. Yu, S. Dong, The influence of crosslink density on the failure behavior in amorphous polymers by molecular dynamics simulations, Materials 9 (4) (2016) 234.
[67] L. Ramos, L. Cipelletti, Intrinsic aging and effective viscosity in the slow dynamics of a soft glass with tunable elasticity, Phys. Rev. Lett. 94 (15) (2005) 158301.
[68] M. Rubinstein, R.H. Colby, Polymer Physics. Chapter 7, Oxford University Press, 2003.
[69] S.S. Kulkarni, N.M. Bayre, K.A. Khan, Modelling visco-hyperelastic response of silicone based elastomers for soft robotics and foldable structure applications, Int. J. Eng. Sci. 211 (2025) 104253.

Author biography

Leonardo Maggioni received M.Sc. degree in mechanical engineering from the Politecnico di Milano, Italy, in 2023, where he is currently pursuing the Ph.D. degree with the Department of Mechanical Engineering. His main research interest involves the design and qualification of measurement systems based on fiber-optic sensors, for biomechanical and structural health monitoring applications.

Emma Lacagnina received M.Sc. degree in biomedical engineering from the Politecnico di Milano, Italy, in 2024, where she is currently pursuing the Ph.D. degree with the Department of Mechanical Engineering. Her main research interest involves the development of measurement systems based on hyperspectral imaging for the characterization of biological tissues and optical phantoms to advance tissue characterization for applications in biorobotics and minimally invasive surgery.

Alfredo Cigada received the Ph.D. degree in applied mechanics from the Politecnico di Milano, Milan, Italy, in 1994. He is currently a Professor of mechanical and thermal measurements with the Politecnico di Milano. He is also a PI of several national and international projects aimed at the development of new sensing systems, data networks, and analysis. His main research interests include the development of new measurement systems for structural health monitoring of civil structures and cultural heritage.

Paola Saccomandi received the Ph.D. degree in biomedical engineering from the Università Campus Bio-Medico di Roma, Rome, Italy, in 2014. Since 2018, she has been an Associate Professor with the Department of Mechanical Engineering, Politecnico di Milano, Milan, Italy. She is a Principal Investigator of three European Research Council Grants and several national/international projects. Her main research interests include fiber-optic sensors for thermal, mechanical, and biomedical measurements, biomedical imaging, and light-based approaches for hyperthermal tumor treatment and monitoring.